Chapter 5

Investigation of the effect of stack plate edge shape upon the performance of a thermoacoustic couple

Previous studies (including the study presented in Chapter 4) have considered the effect of finite plate thickness upon the rate of heat and flow transportation pertaining to the thermoacoustic couple or stack plate (Worlikar et al. 1998, Besnoin 2001). The stack plate was represented by a rectangular section: however in practice, typical parallel plate or spiral stacks do not have perfectly square leading edges, and modern manufacturing techniques permit the design and construction of profiled edges. With existing literature considering only rectangular or zero-thickness (1-D) plates, it would be interesting to see if the heat transfer between the plate and working gas could be improved using non-rectangular cross sections, such as those with round or elliptical stack plate edges. This chapter addresses this very issue.

Section 5.1 outlines the numerical model used, and Section 5.2 presents the variants of edge shape considered in this study, and a brief discussion of the modelspace and parameters used. The performance of each plate edge shape variant is compared using the measures defined in Section 5.2.3. Results using these performance measures are presented in Section 5.3 and are discussed in Section 5.4.

5.1 Numerical model

The numerical model is based upon that used in Chapter 4, with the exception that the fluid-solid boundary representing the stack region is non-rectangular for many of the edge profiles. The thickness of all plates in the centre of the stack region, t_s, is equal to the mean thermal penetration depth $\delta_{\kappa m}$.

5.2 Modelspace

The modelspace used to investigate the effect of different end shapes was adapted from the model used for non-zero thickness stack plates, as shown in Figure 5.1. For all shapes considered here, the overall plate length of L_S=0.252m and the plate thickness t_s at mid-length of 2.4mm were kept constant, to enable comparison with the results of Chapter 4 and to maintain plate-spacing and length scales consistent with the numerical study of Ishikawa & Mee (2002). The edge shapes considered in this study are as follows:

1. **Rectangular** (Figure 5.1(b)): Stack plates which are rectangular in cross section are expected in realised thermoacoustic devices. This model will be used as a benchmark for comparison with zero-thickness stack plates (Figure 5.1(a)) as described previously in Chapter 4.

2. **Rounded edges** (Figure 5.1(c)): The leading and trailing edges of the rectangular stack plate are modified with fillets with radii equal to the plate
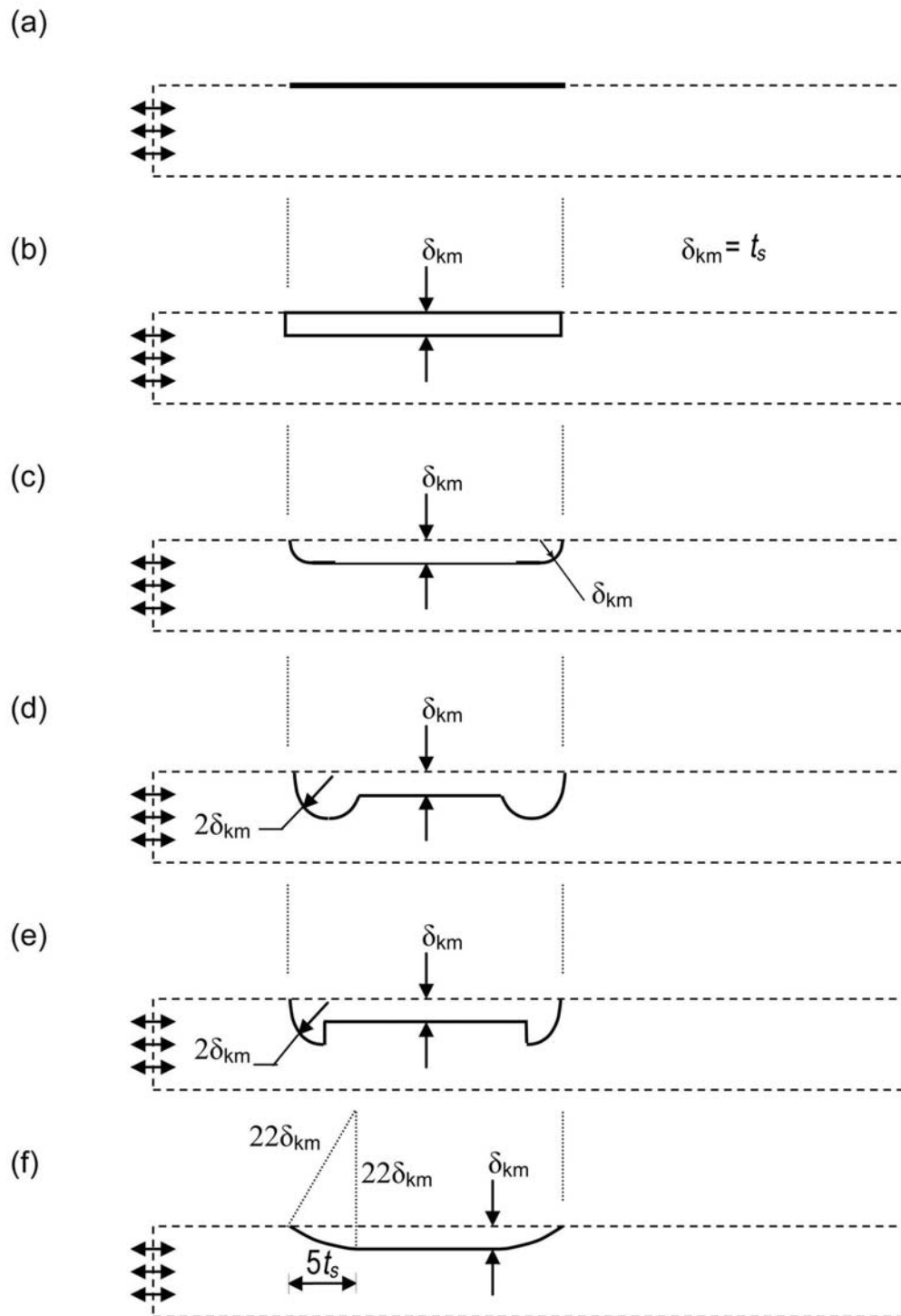
Figure 5.1: Sketches of modelspaces used for modelling different stack end shapes: (a) zero-thickness plates (Ishikawa 1999, Cao et al. 1996), (b) Rectangular (Finite thickness), (c) Rounded edges, (d) Bulbous edges, (e) Talon edges and (f) Aerofoil edges. All modelspaces shown are otherwise identical to that presented in Figure 4.2(c). The thickness of all plates in the centre of the stack region, t_s, is equal to the mean thermal penetration depth $\delta_{\kappa m}$.

thickness t_s are applied to the rectangular stack shape. The elimination of the right-angled edges is anticipated to reduce the flow impedance and flow recirculation near the plate extremities. Rounded edge stack plates could potentially be manufactured using abrasive techniques.

3. **Bulbous edges** (Figure 5.1(d)): The leading and trailing edges of the rectangular stack plate are modified with semi-circular sections with radius equal to twice the plate thickness t_s which are centred $2t_s$ inside each end of the plate. The increased flow impedance at the plate extremities might improve the performance of the stack by 'constraining' fluid parcels within the stack region. In practice a bulbous section could potentially be manufactured by dipping a stack into an adhesive or molten material which would then be allowed to harden into the bulbous edge shape.

4. **Talon edges** (Figure 5.1(e)): The leading and trailing edges of the rectangular stack plate are modified with circular quadrants with radius $2t_s$ which are centred $2t_s$ inside each end of the plate and located such that the chord of each quadrant faces outward from the stack interior. Between the two quadrants is a plate of thickness t_s. This edge shape design was considered as a means to further constrain fluid within the stack region. Larger stacks could potentially incorporate this plate edge shape by attaching suitably shaped tips to the plate.

5. **Aerofoil edges** (Figure 5.1(f)): The leading and trailing edges of the rectangular stack plate are modified with aerofoil tips with a length arbitrarily set to $5t_s$ (i.e. an 'aspect' ratio of 5) added to each end of the plate stack. The edge is implemented in the modelspace using the chord of a circle $22t_s$ in diameter. Minimising the flow impedance presented may result in increased movement of the fluid parcels and transfer of heat down the length of the stack. Aerofoil stack plates for larger thermoacoustic systems could potentially be manufac-

tured with minimal effort using die-forming, injection-moulding systems, or even extrusion of single plates.

The modelspace and computational environment used for this chapter is the same as that described in Chapters 3 and 4, with the shape of region 'P' (Figure 3.1) modified in the current study to model variants of stack plate edges.

The study presented in Section 3.1 found that solver profile 'S2', mesh profiles 'G3' and 'G5' and timescale profile 'T1' struck the most effective balance of computational effort and solution accuracy. Solver profile 'S2' uses second-order discretisation of state variables and a laminar viscous model which relies on good near-wall resolution for effective modelling of the heat transfer rate. The meshes used in this study are summarised in Table 5.1. The circular and curved elements present in many of the modelspaces were achieved by applying triangular mesh elements using default 'PAVE' settings within the *Gambit* (v2.3.16) environment. Mesh spacings along subdomain boundaries were retained for all models considered in this study.

Table 5.1: Grid meshes used for each modelspace in this study. Here, $\delta_\kappa/\Delta y$ is the minimum ratio of thermal penetration depth to grid mesh spacing normal to and within a distance of δ_κ from the heat exchanger surface. Refer to Figure 3.1 for definitions of the grid interval count n. e is the (spatial) ratio used within *Gambit* (*FLUENT 6.2.16 User Manual* 2006) to grade the mesh along each subdomain boundary.

Edge Profile	Node count	n_{xS}	n_y	Typ. $\delta_\kappa/\Delta y$	e_{xA}, e_{xB}
Rectangular	159,418				
Rounded	131,217				
Bulbous	151,579	504	200	$\geq$60	1.0
Talon	150,780				
Aerofoil	139,643				

Non-rectangular quad elements were used to model curved stack plate edges and nodes were concentrated at the stack plate edges. A ratio of $\delta_\kappa/\Delta y =60$ achieved

for the Rectangular model is at least matched or exceeded by the other models studied.

Figure 5.2 shows the typical meshing of each model considered in this study. Based upon the results presented in Chapters 3 and 4, the rate of time-averaged heat transfer and flow disturbance is highest in the vicinity of the stack leading and trailing edges. The mesh density was increased at these locations accordingly, as can be seen in Figure 5.2. The transverse mesh density within the stack plate at distance from the stack edge varies between each model. The variance between meshes is not considered significant because the rate of heat transfer distant from the stack edges is relatively minimal and any internal temperature distributions should be insignificant within the timeframes under consideration.

Inspection of Table 5.1 shows a significantly higher node count for the Rectangular model over the other models considered, however the additional nodes are located deep inside the stack region within the stack material (*c.f.* Figures 5.2(a) and 5.2(b) or 5.2(c)). The influence of these additional nodes is considered to be negligible since the expected time-averaged heat flux across these interfaces is concentrated at the edges, not deep inside the stack region.

5.2.1 Operating conditions

Table 5.2 presents the operating conditions for each run considered in this study. To investigate the influence of stack plate edge shape, each of the modelspaces shown in Figure 5.1 are compared for identical global operating conditions and increasing drive ratio DR. Runs 11 to 20 use a drive ratio above 3% to provoke a siginificant increase in non-linear effects associated with the flow impedance of each edge shape. Following the discussion of turbulence criteria in Section 4.1.3.1, the streaming Reynolds number $N_{R,S}$ was restricted to less than $(200)^2$. Above
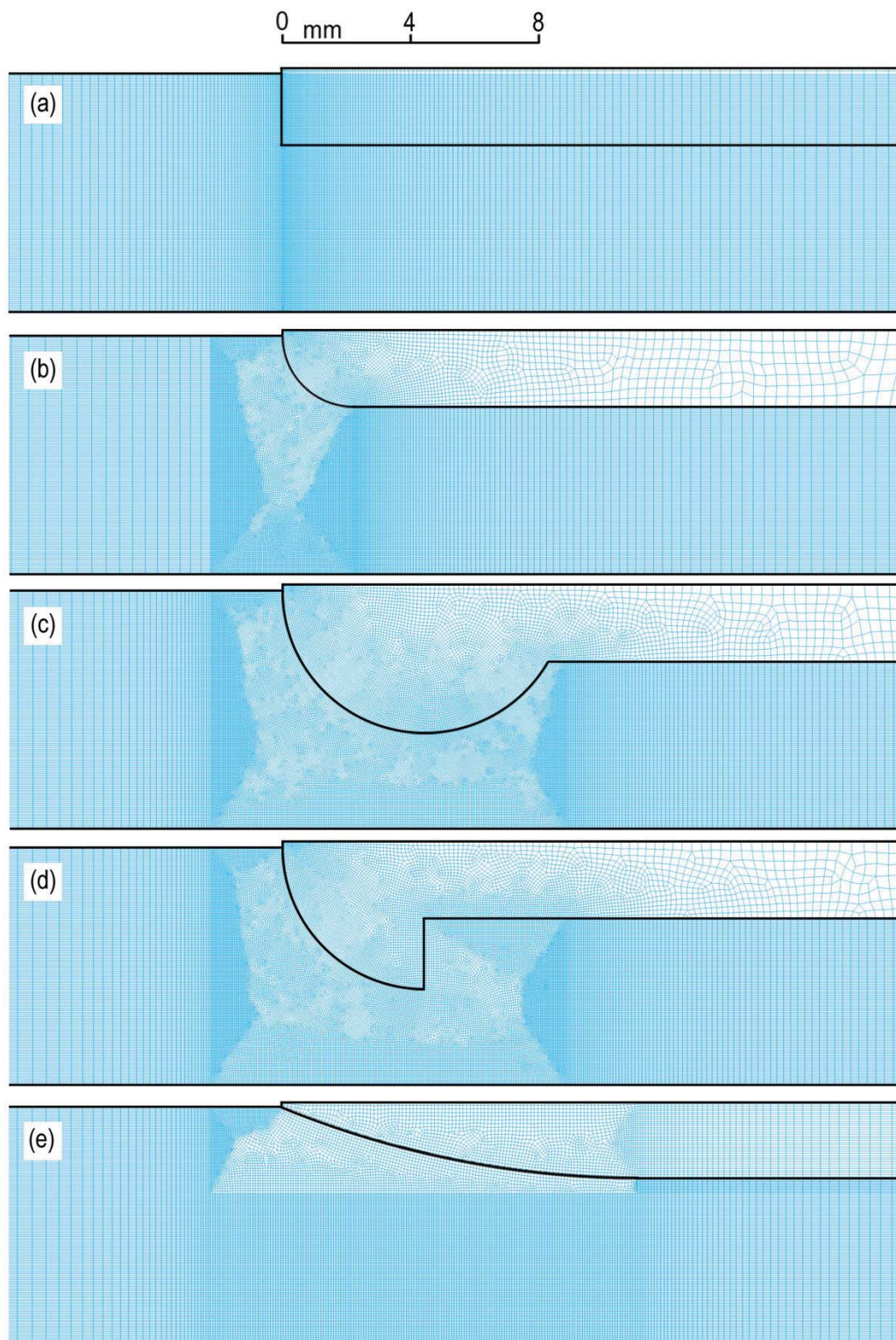
Figure 5.2: Close-up view of the grid meshes for (a) Rectangular, (b) Rounded, (c) Bulbous, (d) Talon and (e) Aerofoil edge shape models at the 'cold' end of the stack region ($x \sim 0$). All five meshes shown are at the relative scale indicated.

Table 5.2: Run number for stack plate edge shape and drive ratio. For all runs, $t_s=\delta_{\kappa m}=0.024$m, $BR=0.7$ at plate midlength.

Edge Shape	$|p_1|/p_m$ (%)			
(Figure 5.1)	1.7	3.4	5.1	6.8
Rectangular	1	6	11	16
Rounded	2	7	12	17
Bulbous	3	8	13	18
Talon	4	9	14	19
Aerofoil	5	10	15	20

$N_{R,S}$ values of $(200)^2$, the flow is considered to have transitioned to a turbulent flow regime and therefore exceeded the capacity of the chosen simulation parameters.

For all runs in this chapter, $t_s=\delta_{\kappa m}=0.024$m in the plate midsection which leads to a blockage ratio BR of 0.7. The length of the stack plate is the same as in Chapter 4, i.e. $L_S=0.252$m.

Following the method described in Chapter 3, the thermoacoustic couple is driven using a standing acoustic wave of amplitude $|p_1|$ and simulated for 20 periods of oscillation (0.2s) at which point each model was found to operate at 'limit state' as defined in Section 3.2.2.1.

5.2.2 Material properties

Table 5.3 lists the physical properties used in each simulation, which differ from those used for the previous results presented in Chapter 4 in that the temperature dependence of gas thermal conductivity k_0 and dynamic viscosity μ are modelled using a linear piecewise approximation based upon published values according to temperature (Mills 1999). For comparison with results obtained in previous studies, consistent material properties and acoustic conditions are retained where possible. The use of helium at $\sim$10% atmospheric pressure as the working fluid also enables comparison with the results of Ishikawa and Mee (Ishikawa & Mee 2002), albeit

for the zero-thickness stack plate used in their work. The density of the gas is calculated using an ideal gas approximation.

Table 5.3: Flow conditions and material properties used for all computational runs presented in Chapter 5.

Property	Value	Units
Operating frequency, f	100	Hz
Ambient temperature, T_m	300	K
Mean pressure, p_m	10	kPa
Gas properties: Helium		
Prandtl number, σ	0.69	
Thermal conductivity, k_0	Piece-wise linear approx. (Mills 1999, Table A-7)	W/mK
Dynamic viscosity, μ	Piece-wise linear approx. (Mills 1999, Table A-7)	N·s/m^2
Heat capacity, c$_p$	5,193	J/kgK
Ratio of specific heats, γ	1.665	
Plate material properties:		
Thermal conductivity, k_s	10	W/mK
Heat capacity, c$_{ps}$	400	J/kgK
Density, ρ_s	400	kg/m^3

The density of the solid material is set lower than that expected in practical devices, to exaggerate any internal temperature differentials obtained in the study such that they can be more easily observed during the simulation timeframe, whilst maintaining a thermal capacity significantly higher than that of the oscillating gas.

5.2.3 Performance measures

The influence of the shape of the edge of the stack plate will be assessed using the performance metrics discussed in the following subsections. The statistical uncertainty of the results is described in Section 3.2.1.2.

5.2.3.1 Heat transfer

The distribution of time-averaged heat flux density over an oscillatory cycle at a fluid-solid boundary, $\left\langle \dot{h}_y \right\rangle$, is a useful performance measure that has been used in

the majority of past studies of thermoacoustic couples. In previous studies which considered a stack plate of zero thickness (Cao et al. 1996, Ishikawa & Mee 2002, Piccolo & Pistone 2006), this quantity was also referred to as a time-averaged heat flux in the transverse or y-direction, which is here represented by $\left\langle \dot{h}_y \right\rangle_t$. The term $\langle \dot{h}_{hx} \rangle_t$ will refer to the time-averaged heat flux through all fluid-solid boundaries of the stack plate and includes heat transfer in the axial direction, $\left\langle \dot{h}_x \right\rangle_t$.

In this study, where the heat exchanging surfaces of the stack plate are not orthogonal, it is important to define the heat flux through the plate surface using vectors normal to the heat exchanger surface S as shown in Figure 5.3.
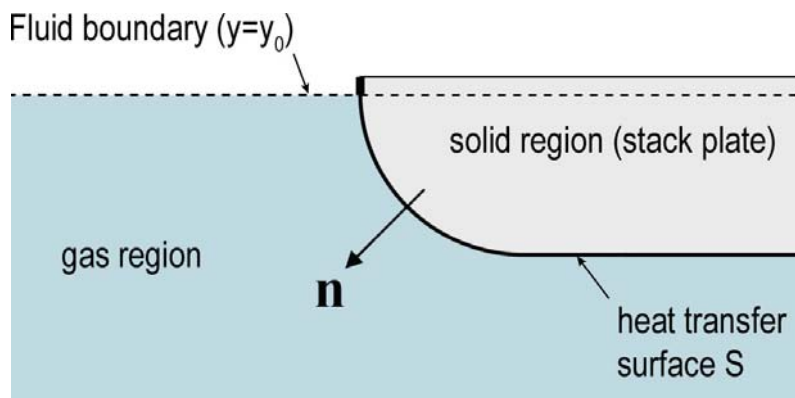
Figure 5.3: Example normal unit vector $\hat{\mathbf{n}}$ to the heat exchanger surface S.

The integral of heat flux $\dot{h}$ through the plate surface S is therefore defined as

$$\dot{h}_{hx} = \dot{h}_S = \int_S \mathbf{\dot{h}} \cdot d\mathrm{A} \tag{5.1}$$

and represents the heat flux normal to the plate surface. However, this value can be misleading as it combines negative heat flux (i.e. cooling of the surrounding gases) as well as positive heat flux. Conservation of energy requires that for a domain of constant temperature that is fully insulated and/or enclosed by surface S, the sum of heat flux $\dot{h}$ over the surface S is zero. In practice though, the

internal temperature of the stack plate varies within the plate despite all surfaces at solid-fluid boundaries being fixed at 300K. Entropic losses are also included in the model and are expected to create minor additional heat flux which is included in the integral of Equation (5.1).

An improved method is to treat the stack region as comprising only two surface groups: a 'cold' surface in which the time-averaged heat flux is negative; and a 'hot' surface for which the time-averaged heat flux is positive. A point on the surface S at which the time-averaged heat flux at limit state is zero is used to divide the stack plate into 'cold' and 'hot' ends or regions. Figure 5.4 illustrates this method for an arbitrary thermoacoustic couple plate surface. As indicated in this figure, the 'cold end' corresponds to the section of plate for which $\langle \dot{h} \rangle_t < 0$ at the solid-fluid boundary, and its axial length is denoted by $L_{S,\text{cold}}$. Similarly for $\langle \dot{h} \rangle_t > 0$ on S at the 'hot end' spanning $L_{S,\text{hot}}$ where $L_s = L_{S,\text{cold}} + L_{S,\text{hot}}$. The surfaces on S for which $\langle \dot{h} \rangle_t < 0$ and $\langle \dot{h} \rangle_t > 0$ are denoted by S_{cold} and S_{hot} respectively. For more complex surfaces, S_{cold} and S_{hot} may not be continuous, as will be shown for the Talon edge model in Section 5.3.2.
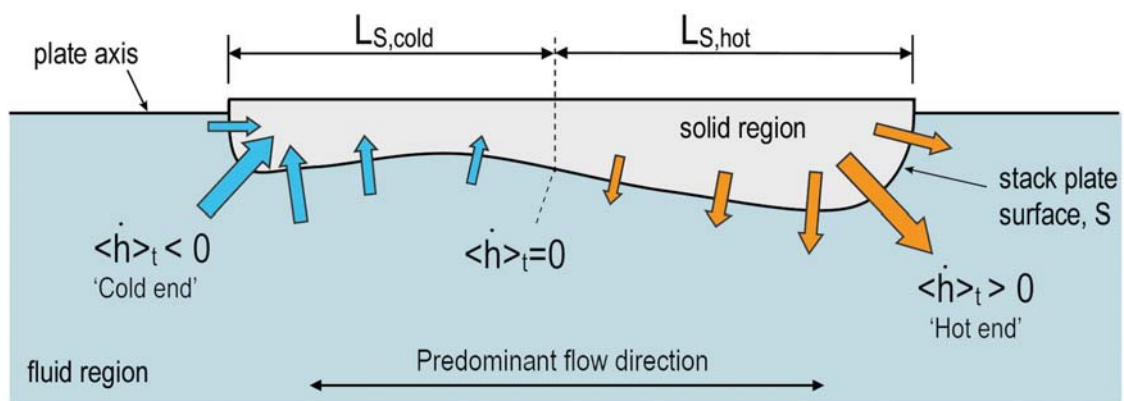

Figure 5.4: Diagram of a thermoacoustic couple with arbitrarily shaped heat exchanger surface S.

As shown in Figure 5.4, this approach sets the boundary between the 'cold' and

'hot' ends of the plate as being straight and perpendicular to the predominant flow vector. In practice, this boundary may be distorted from a straight line.

The performance measure considered here is therefore the total time-averaged thermal power transferred from the cold section of the plate per unit width, or

$$\dot{Q}_{S,\text{cold}} = \int_{S_{\text{cold}}} \dot{\mathbf{h}} \cdot d\mathrm{A}. \tag{5.2}$$

5.2.3.2 Temperature differentials

The time-averaged difference in area-weighted average gas temperature at $x=0$ and $x=L_S$ is given by

$$\Delta T_{k,hx} = \left\langle \left(|T_k|_{x=L_S} - |T_k|_{x=0} \right) \right\rangle_t \tag{5.3}$$

and could be considered the axial gas temperature difference across the heat exchanging surface, hence the subscript 'hx'.

Experimental studies of thermoacoustic couples often cite the 'edge-to-edge' temperature difference as a performance metric (Wheatley et al. 1983) and $\Delta T_{k,hx}$ is here considered to be its numerical equivalent.

5.2.3.3 Acoustic power input to the system

Each stack edge profile presents a different input acoustic impedance to the acoustic source. Hence the amount of acoustic power delivered to each system will vary. To enable comparisons between the different systems, the performance measures $\Delta T_{k,hx}$ and $\dot{Q}_{S,\text{cold}}$ are normalised by the time-averaged acoustic power $\dot{E}_2$ input to the system, the calculation of which is detailed below.

Considering that all solid external boundaries to the thermoacoustic couple model are thermally insulated, it follows that the time-averaged net acoustic power absorbed by the system is equal to $\dot{E}_2$ on the inlet boundary. In this study this single inlet to the domain comprises 100 face elements and is of sufficient proximity to the stack region for the velocity field to contain significant transverse velocity components. Therefore, the acoustic power input to the system will need to be calculated using a surface integral approach.

The boundary 'INLET' is located at the left edge of the thermoacoustic couple model as shown in Figure 5.5.
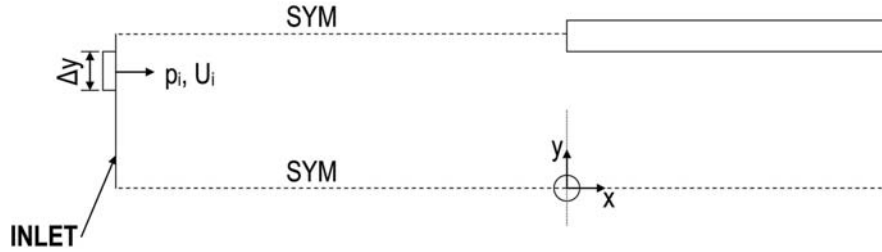
Figure 5.5: Arrangement and parameters used to determine the acoustic power $\dot{E}_2$ within the *Fluent* CFD environment, using pressure p_i and volume velocity U_i obtained at the ith segment of boundary 'INLET'.

On the inlet boundary shown in Figure 5.5, the pressure is set to

$$p|_{\text{INLET}} = |p_1| \sin(kx') \sin(\omega t) \tag{5.4}$$

and 1-D volume velocity response at limit state is therefore

$$U|_{\text{INLET}} = |U_1| \cos(\omega t + \phi_{pU}). \tag{5.5}$$

where x' is the distance to the centre of the resonator, as shown in Figure 4.1, such that the term $\sin(kx')$ is used to achieve $|p_1|$ at the resonator terminations. ϕ_{pU} represents the phase angle between pressure and volume velocity.

With this information, $\dot{E}_2$ is defined by (Swift 2002, Equation 5.3)

$$\dot{E}_2 = \frac{1}{2} Re\left\{p_1 U_1^*\right\} = \frac{1}{2} Re\left\{p_1^* U_1\right\} \tag{5.6}$$

where the asterisk (*) indicates complex conjugate, or (Swift 2002, Equation 5.4)

$$\dot{E}_2 = \frac{1}{2} |p_1| |U_1| \cos\phi_{pU}. \tag{5.7}$$

However, pressure and velocity data is real within the *Fluent* environment and it is therefore difficult to estimate $\dot{E}_2$ based upon Equations (5.6) or (5.7). Applying Equation (5.5) using curve-fitting techniques to determine the phase angle ϕ_{pU} is difficult with transverse velocity components on INLET. However, by assuming the time-averaged axial position of fluid along the boundary coincides with the boundary itself, the acoustic power is estimated using (Swift 2002, Equation 5.6)

$$\dot{E}_2 = \frac{\omega}{2\pi} \oint pU \ dt \tag{5.8}$$

or with fixed time step size and Δy on the inlet boundary,

$$\dot{E}_2 = f \int \int_{\text{INLET}} pU \ dy \ dt \tag{5.9}$$

which can be obtained from the *Fluent* environment using a custom field function. Although the pressure amplitude and hence drive ratio is set equal in each model, the difference in acoustic velocity fields will require that $\dot{E}_2$ be used to normalise the results obtained.

5.2.3.4 Coefficient of performance

The coefficient of performance of the thermoacoustic couple is defined here as

$$COP = \frac{\dot{Q}_{S,\text{cold}}}{\dot{E}_2} \tag{5.10}$$

with $\dot{E}_2$ representing the time-averaged acoustic power input to the system, as calculated using Equation (5.9).

5.3 Results

In the following subsections each edge shape will be compared on the basis of effective heat transfer, cooling power, temperature distribution and overall efficiency.

5.3.1 Flow structures

Pathlines for t=0.2s are presented for the Rectangular, Rounded, Bulbous and Talon edge profiles in Figures 5.6 and 5.7 for drive ratios of 1.7% and 5.1% respectively. The pathlines presented in these figures are coloured by velocity magnitude. As expected, flow velocities in the vicinity of the stack plate edge are reduced from that expected using the Rectangular edge profile by using the 'sleeker' Rounded and Aerofoil edge shape profiles. Compared to the Rectangular edge shape, flow velocities in the vicinity of the plate edge are significantly higher for the broader Talon and Bulbous edge shape profiles, as expected because of their increased blockage of the flow.

Flow recirculation zones develop on the inside face of the stack region for the Rectangular, Talon and Bulbous edge shape profiles, although the recirculation zones are significantly larger for the Talon and Bulbous edge shape profiles at the instant of time shown in Figures 5.6 and 5.7. At a drive ratio of 5.1%, a recirculation

pattern outside the stack region is evident for the Bulbous (Figure 5.7(c)) and Talon (Figure 5.7(d)) edge shape profiles. At the instant of time shown, this recirculation zone is moving downward and close to collapse, but is still present at this time frame for these two edge shape profiles. This is because the acoustic phasing is upset by the presence of the flow blockage. Gas flow exiting the stack region is slowed and delayed as it negiotiates the stack edge, entraining flow moving rightward. This generation of flow vortices outside the stack region has been discussed in Chapter 4 for the Rectangular edge shape profile. Similar recirculation zones also develop for the Rounded and Aerofoil edge shape profiles, albeit for much shorter timeframes and over smaller areas.

The recirculation zones shown outside the stack region in Figures 5.7(c) and 5.7(d) also develop using a drive ratio of 1.7%, but the recirculation zone disappears immediately prior to the time instant shown. The flow outside the stack region instead appears slightly curved in Figures 5.6(c) and 5.6(d) as a result.

Figures 5.8 and 5.9 present the evolution of flow pathlines for the Talon edge shape profile at a drive ratio of 1.7%. Pathlines are presented in 36° or 0.001s increments and show the development of recirculation zones both internal and external to the stack region. In similar fashion to the data presented in Chapter 4 for the Rectangular edge shape profile, recirculation zones develop near the plate axis ($y=y_0$) and move downward towards the plate midspacing ($y=0$) and collapse. However, further in contrast to results presented in the previous chapter, *two* recirculation zones develop on the inside of the stack region per acoustic cycle. The recirculation zone clearly visible in Figures 5.8(a) to 5.8(d) and also in Figure 5.9(e) is first detected using pathline imagery at a phase ϕ of 295.2° ($t=0.1982$s) and is found to have completely dissipated at $\phi=113.4°$ ($t \approx 0.2032$s), or nearly one half period later.

The 'secondary' recirculation zone seen in Figure 5.9(c) and believed to have developed from separation of flow exiting the stack region, is visible between ϕ=228.6° ($t \approx$0.2064s) and ϕ=280.8° (t=0.2078s), or for roughly 15% of the acoustic cycle. Interestingly, this additional recirculation is slightly beneficial at this drive ratio, because it increases the rate of mixing and hence heat transfer over this small section of the stack.

5.3.2   Heat transportation

Figures 5.10 and 5.11 present surface plots of the shift in normalised heat transfer flux $\dot{h}_S$ for Runs 2 and 4 respectively. The heat transfer rate is normalised using the method described in Appendix C.1 to remove bulk gas compression effects. The influence of the edge shape is clearly evident in each figure. For the Rounded edge profile, where the recirculation of fluid near each edge is minimal, the surface contour of $\dot{h}_S$ is relatively smooth. At the cold end of the stack plate ($x/L_S \sim$0), normalised $\dot{h}_S$ is always negative for the Rounded edge shape but not so for the Talon edge profile. Strong gradients in $\dot{h}_S$ develop on the inside vertical edge of the Talon edge shape (indicated with symbol $\diamondsuit$ in Figure 5.11), particularly at the phase corresponding to t=0.2075s. At this phase, the $\dot{h}_S$ is strongly negative (effective cooling) at the bottom 'tip' of the Talon edge shape, but also positive (undesired heating) in the upper 'crevice' or corner of the same edge. This range of $\dot{h}_S$ values is significantly higher than that determined over the rounded section of the Talon edge profile (indicated with symbol $\triangle$ in Figure 5.11).

The 'secondary' internal recirculation zone shown in Section 5.3.1, which develops on the inside of the stack region is shown in Figure 5.11 to be beneficial in increasing heat transfer from the plate. On the hot side of the stack region, the small increase in effective heat transfer corresponding to the small secondary recirculation zone which develops is indicated with an asterisk ($*$). On the cold
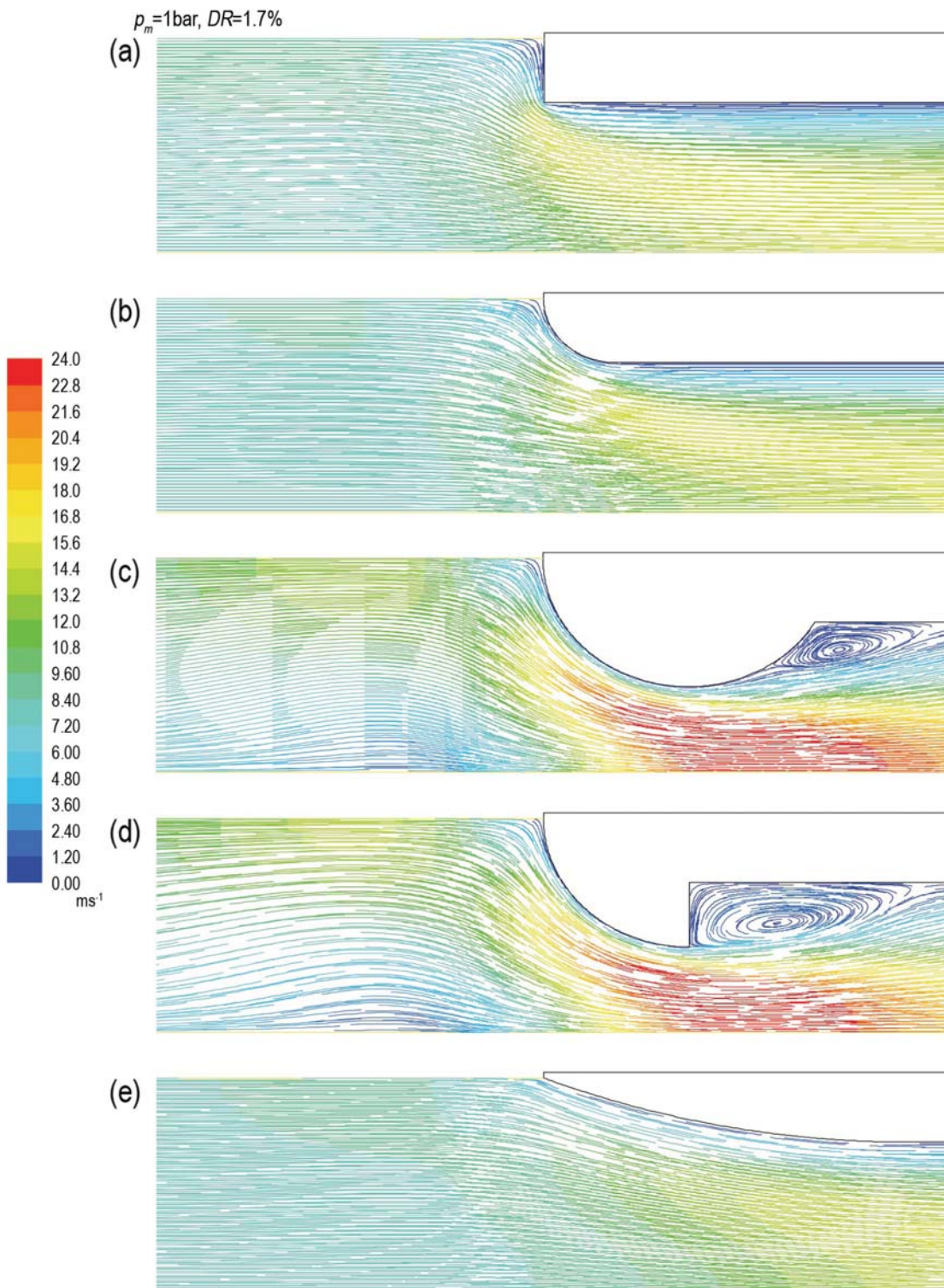
Figure 5.6: Pathlines coloured by velocity magnitude for (a) Rectangular (Run 1), (b) Rounded (Run 2), (c) Bulbous (Run 3), (d) Talon (Run 4) and Aerofoil (Run 5) edge shape profiles at time t=0.2s. DR=1.7%.
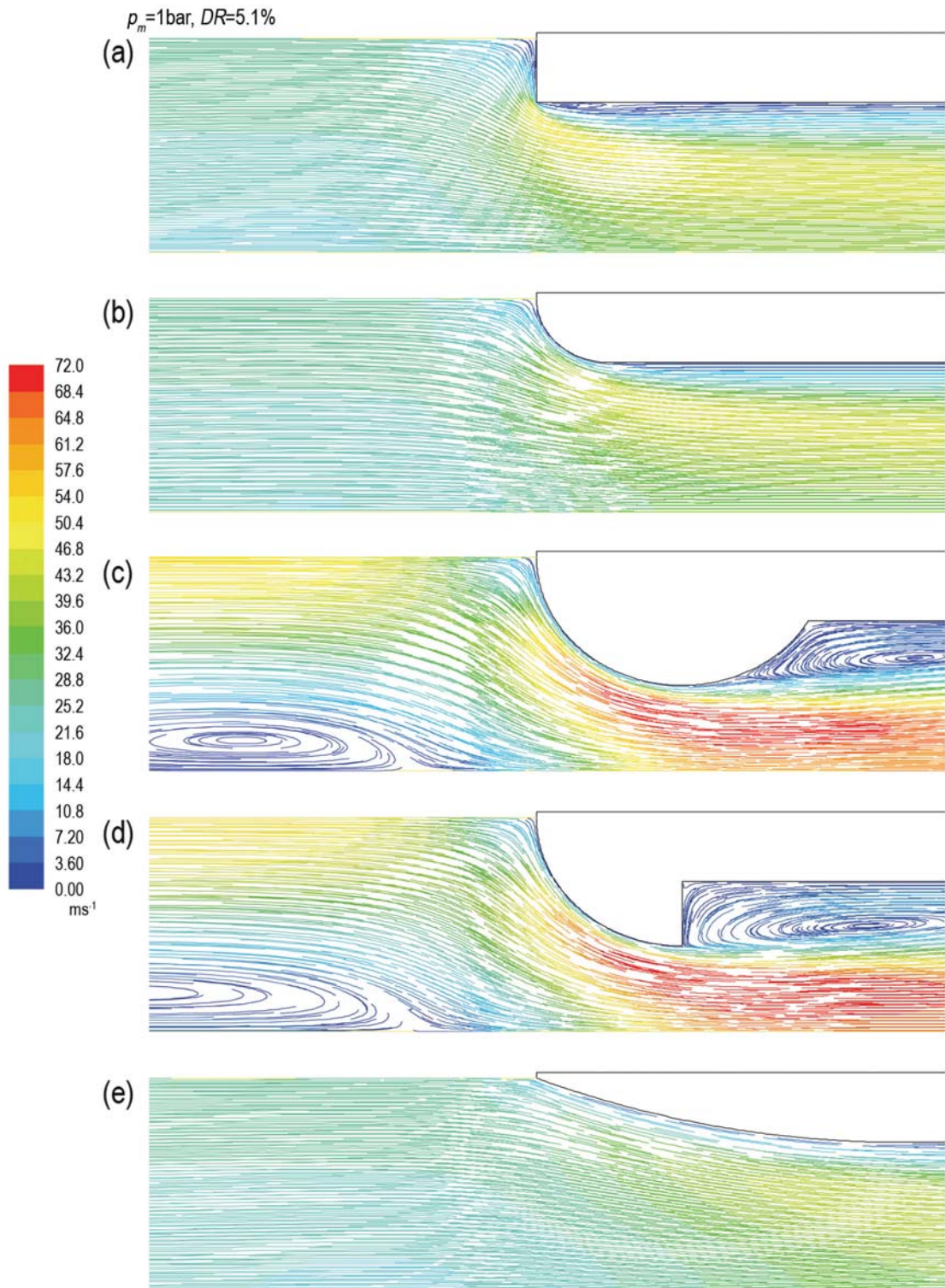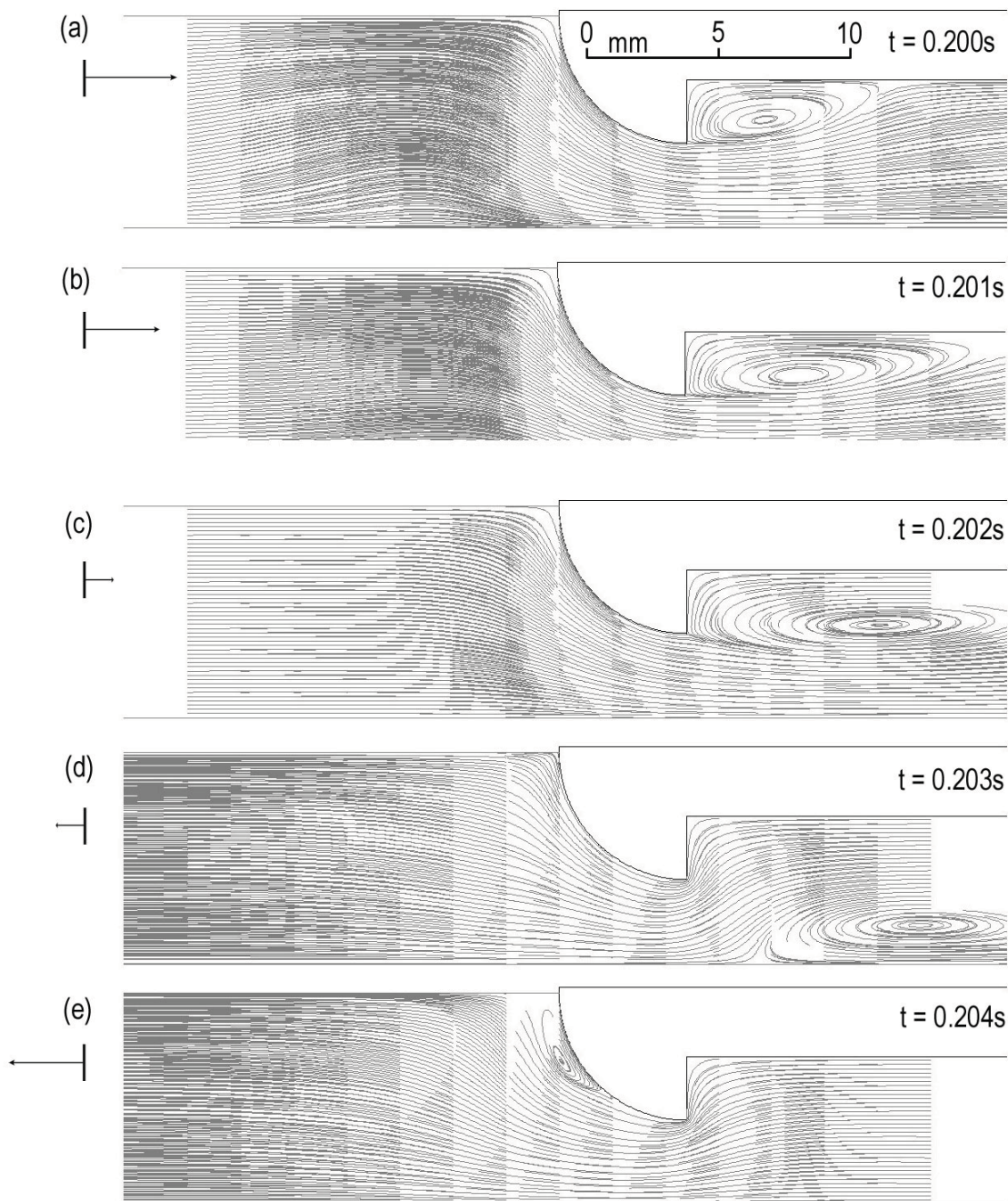
Figure 5.7: Pathlines coloured by velocity magnitude for (a) Rectangular (Run 11), (b) Rounded (Run 12), (c) Bulbous (Run 13), (d) Talon (Run 14) and Aerofoil (Run 15) edge shape profiles at time t=0.2s. DR=5.1%.

Figure 5.8: Flow pathlines for Run 4, DR=1.7%, at (a) t=0.200s, (b) t=0.201s, (c) t=0.202s, (d) t=0.203s and (e) t=0.204s. The prevailing flow direction and velocity magnitude are indicated to the left of each figure.
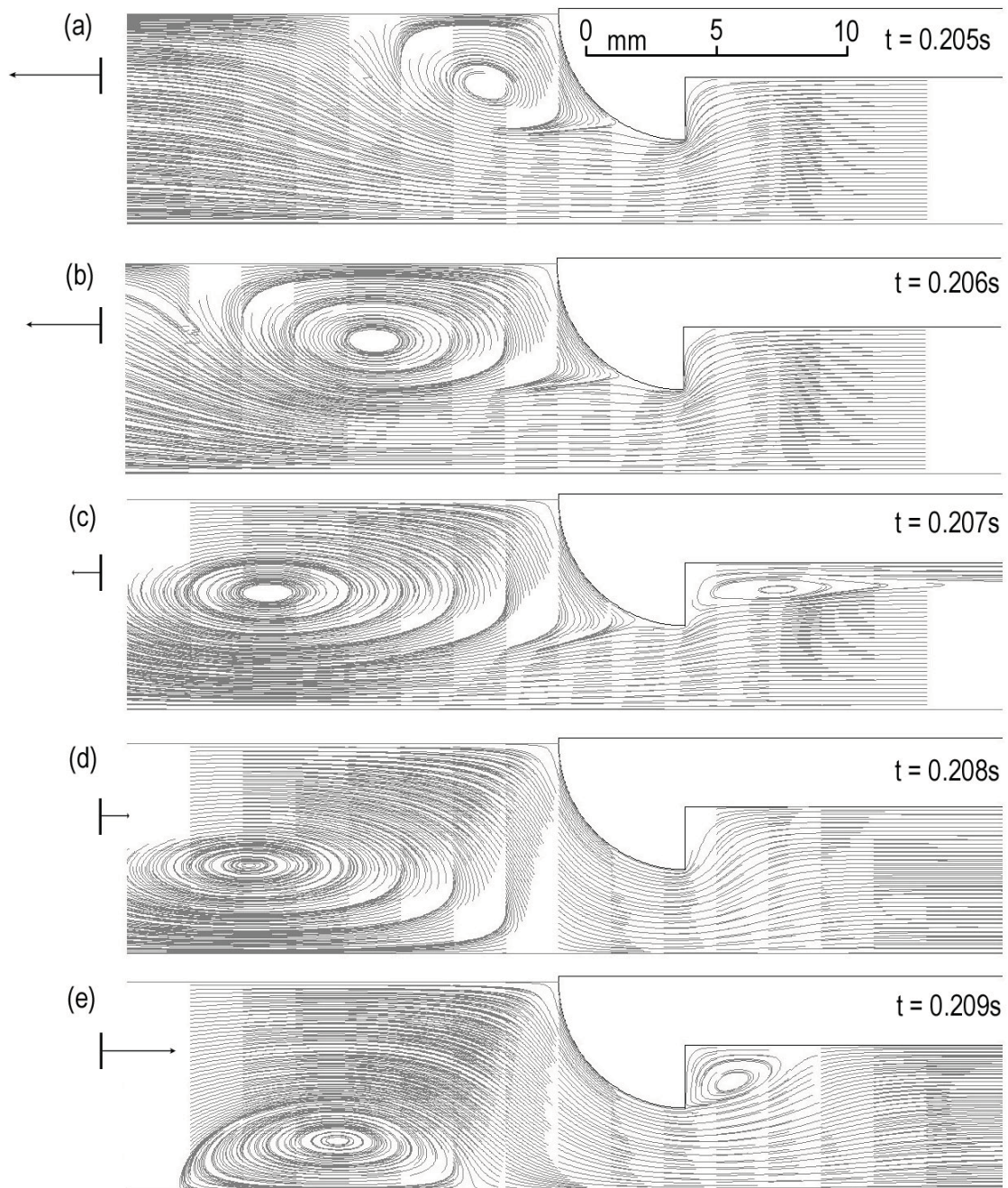
Figure 5.9: Flow pathlines for Run 4, DR=1.7%, at (a) t=0.205s, (b) t=0.206s, (c) t=0.207s, (d) t=0.208s and (e) t=0.209s. The prevailing flow direction and velocity magnitude are indicated to the left of each figure.

side of the stack it is hidden in the figure but is present in the timeframe $t \approx 0.2064$s to $t \approx 0.2078$s. In Section 5.3.3 the overall sum of $\dot{h}_S$ over $L_{S,cold}$ for the Talon edge profile is demonstrated to be actually higher than for the Rounded edge model at a drive ratio of 1.7%, despite a local zone of undesired 'heating' on the inside face of the cold end of the stack plate for the former.

Figure 5.12 shows a surface plot of the normalised heat transfer rate $\dot{h}_S$ for the Aerofoil edge profile at a drive ratio of 1.7% (Run 5). This surface plot shows that the rate of heat transfer across the 'cold' end of the Aerofoil edge profile is significantly lower than that obtained using the other edge profiles considered in this study. This is attributed to the relatively smaller volume of solid at each end of the plate. The rate of heat transfer from the 'hot' end to the gas is however of similar order to the other edge profiles considered.

Figure 5.13 presents the integral of the time-averaged heat flux normalised by that result obtained using the Rectangular edge shape, versus the ratio of acoustic power input $\dot{E}_2$, normalised by the result of Run 1. At a drive ratio of 1.7%, where $\dot{E}_2/\dot{E}_2\big|_{\text{Run 1}} \approx 1$, all four alternative stack plate edge shapes achieve a higher rate of heat transfer in comparison to the Rectangular shape section. However, at a drive ratio of 6.8%, the Talon, Bulbous and Aerofoil edge shapes underperform despite higher acoustic power inputs.

The Rounded edge shape performs noticeably differently to the other edge shapes considered in that it is more effective than the Rectangular edge shape for all drive ratios modelled. It was expected that this result would also be achieved using the Aerofoil edge shape, since both the Aerofoil and Rounded edge shapes present curved edges to reduce flow impedance. However, Figure 5.13 suggests that this is only true for a low pressure amplitude, with the the Aerofoil edge shape
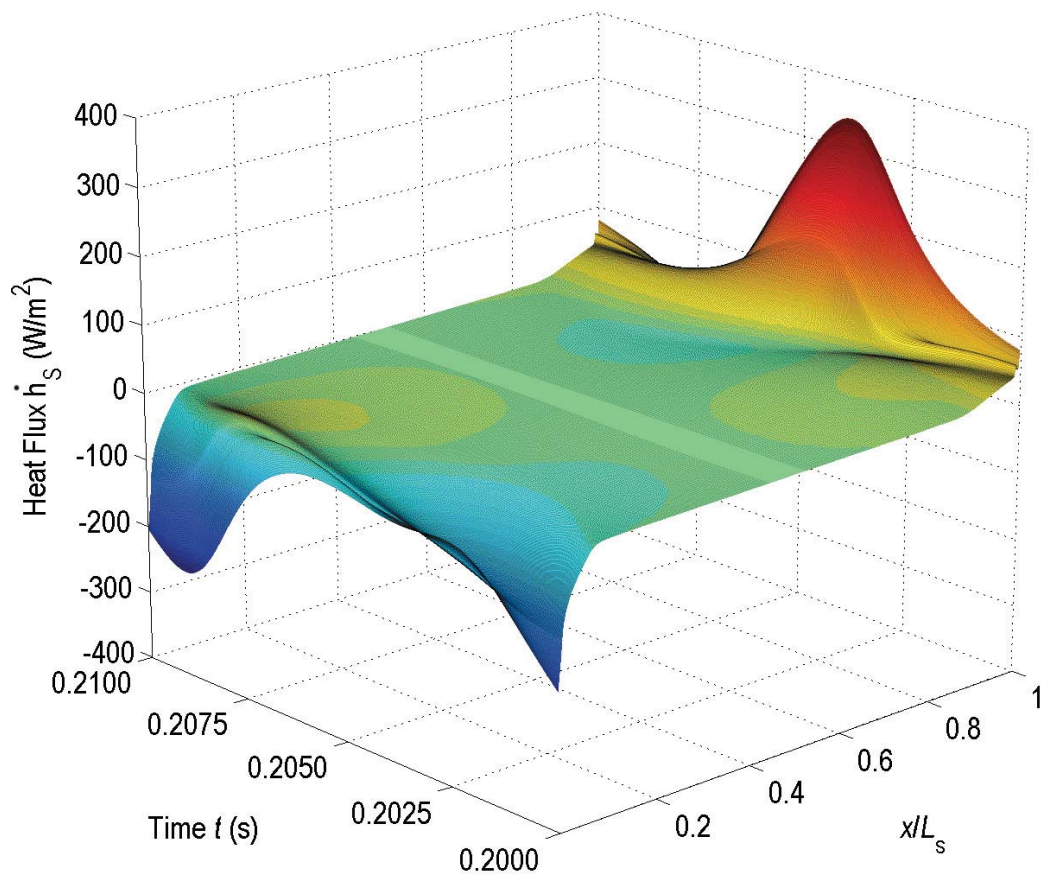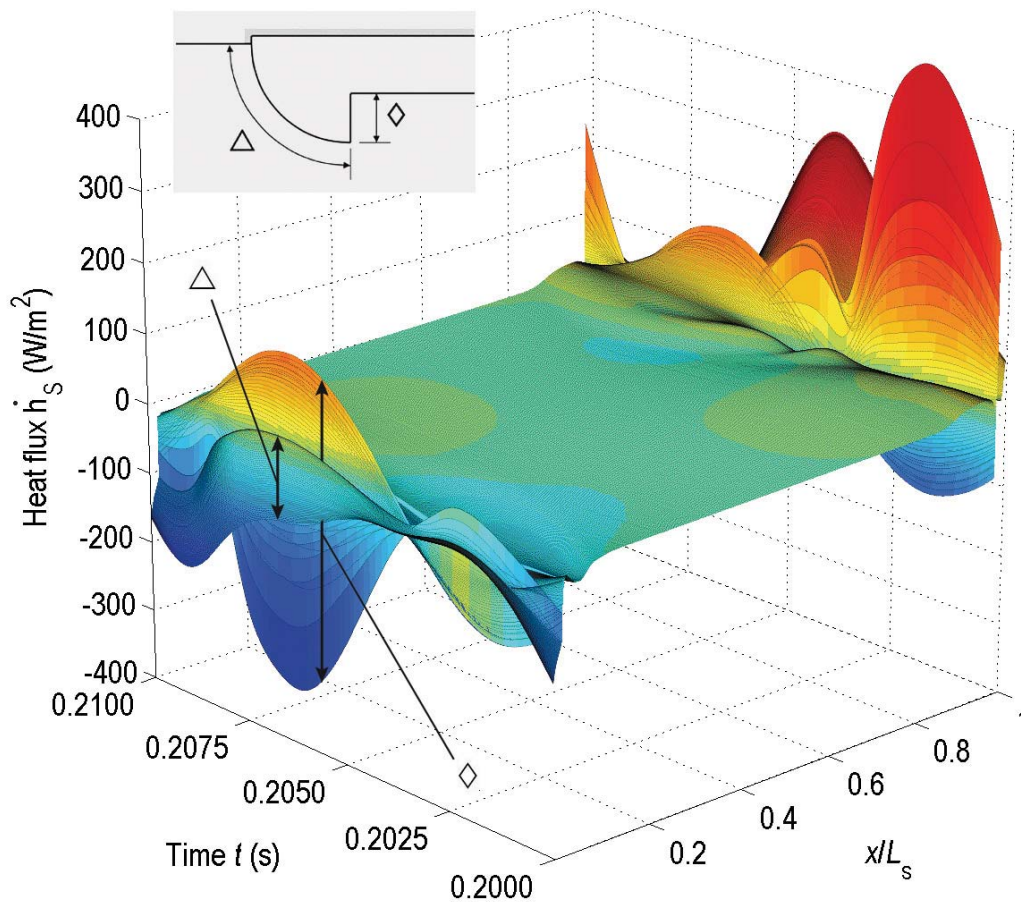
Figure 5.10: Surface plot of normalised heat flux $\dot{h}_S$ for the Rounded stack plate profile using a drive ratio of 1.7% (Run 2).

result deviating from the Rounded edge shape result at drive ratios of 5.1% and 6.8%.

Drive ratios of 1.7%, 3.4%, 5.1% and 6.8% were considered in this study. The time-averaged heat flux is plotted for drive ratios of 1.7% and 6.8% for all stack plate edge shapes considered in Figures 5.14 and 5.15 respectively, which reveal a dramatic difference in $\langle \dot{h}_{hx} \rangle_t$ obtained using the Bulbous and Talon edged shapes, with vertical 'spikes' in the time-averaged heat flux inside the stack region. The corner intersection or crevice on the inside of the stack region is a location of poor effective heat transfer, and when considered over a full period, its effect is counter-productive to the desired thermoacoustic effect. This effect demonstrated using the Bulbous edge shape is exaggerated by the Talon edge shape. Figures 5.16 and 5.17 show this in closer detail of the left ('cold') end of the stack plate. Despite this

Figure 5.11: Annotated surface plot of normalised heat flux $\dot{h}_S$ for the Talon stack plate profile using a drive ratio of 1.7% (Run 4). ($\triangle$) indicates the range of heat flux attributed to the rounded surface on the cold side of the stack plate. ($\diamondsuit$) indicates the range of heat flux attributed to the vertical internal surface on the left side of the stack plate. ($*$) indicates the additional heat transfer at the 'hot end' of the stack due to the 'secondary' recirculation zone which develops on the inside of the stack edge.

effect occurring at all the drive ratios simulated, the overall value of $\langle \dot{h}_{hx} \rangle_t$ is shown in Figure 5.13 to be highest for the Talon and Bulbous edge shapes at a DR of 1.7%.

Whilst Figure 5.13 shows the Bulbous and Talon edge shapes to be more effective in increasing the total rate of effective heat transfer at a DR of 1.7%, Figures 5.14 to 5.17 show ineffective or adverse performance (marked with $*$) near the 'crevice' of the edge feature inside the stack region. At a drive ratio of 1.7%, the Bulbous and Talon edge shapes are shown in Figure 5.16 to result in a smaller
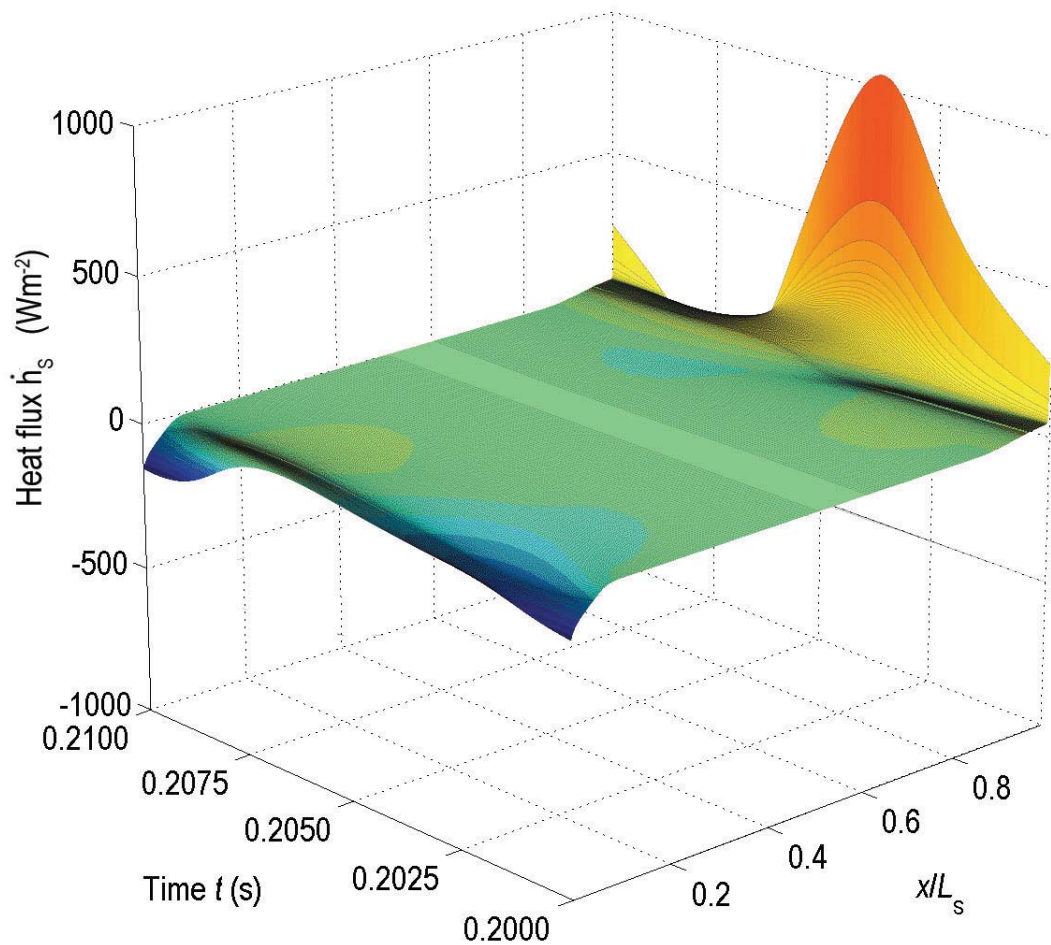
Figure 5.12: Surface plot of normalised heat flux $\dot{h}_S$ for the Aerofoil stack plate profile using a drive ratio of 1.7% (Run 5).

magnitude of $\langle \dot{h}_{hx} \rangle_t$ over the inside 3% to 10% of stack length. This deficiency is larger at higher drive ratios, as shown in Figures 5.15 and 5.17, although the stack length over which this deficiency is evident is significantly larger on the cold side of the stack than on the hot side.

Figures 5.14 and 5.16 show that over each outer 10% of the stack plate length, the Rounded and Aerofoil edge shapes are shown to induce greater $\langle \dot{h} \rangle_t$ than the Rectangular edge shape. At other stack locations, these three edge shapes are shown to achieve near identical values of $\langle \dot{h} \rangle_t$. However according to Figure 5.13, the Bulbous and Talon plate edge shapes achieve a higher total time-averaged heat flux at a drive ratio of 1.7%. This is because these two stack plate edge shapes have
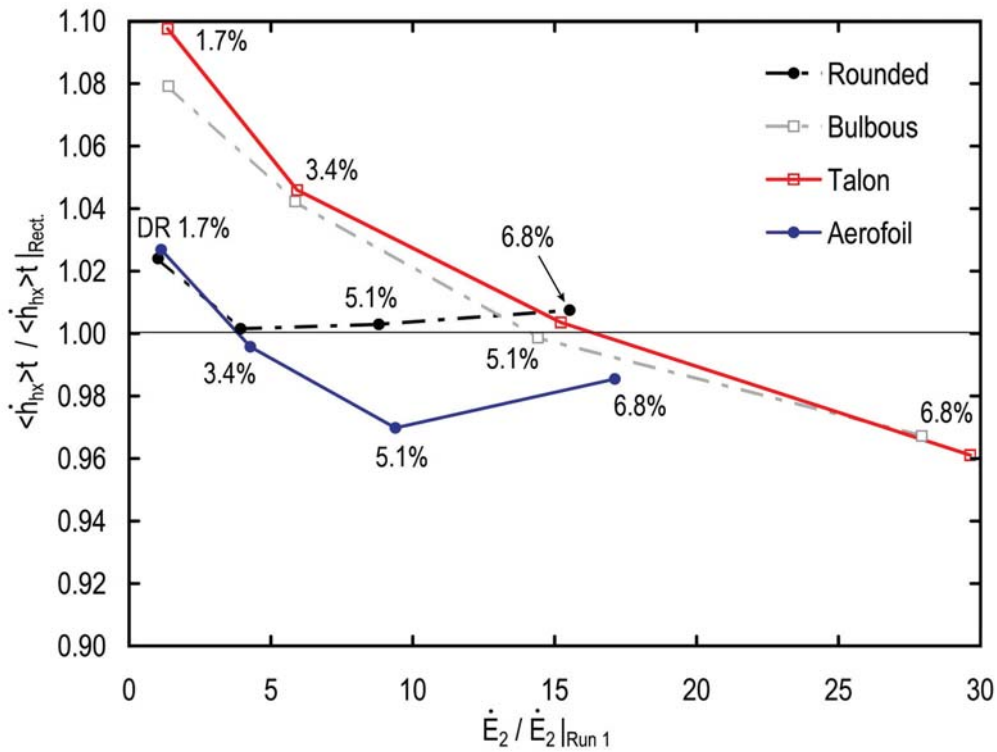
Figure 5.13: Time-averaged heat flux across the stack plate surface $\langle \dot{h}_{hx} \rangle_t$ (normalised using rectangular edge shape result) versus $\dot{E}_2$ normalised by the result of Run 1. Four points of increasing DR (left to right) are plotted for each edge shape modelled.

a greater surface area at the edges where the rate of heat transfer is concentrated, and the flow disturbance due to the greater surface area is not excessive.

Figures 5.18 and 5.19 show the relative distribution of $\langle \dot{h} \rangle_t$ over the Talon edge surface for drive ratios of 1.7% (Run 4) and 6.8% (Run 19) respectively. These two figures show that as the drive ratio is increased, the distribution of effective heat transfer shifts to the tip of the protruding edge. The distribution of $\langle \dot{h} \rangle_t$ is noticeably more perturbed on the rounded leading edge. As discussed previously and indicated (*) in Figures 5.16 and 5.17 at $x/L_S \approx 0.019$, $\langle \dot{h} \rangle_t$ is positive in the 'crevice'. The Bulbous edge shape, which also features a large protusion at the stack plate edge, also results in a severe shift in $\langle \dot{h} \rangle_t$ at the 'crevice', although not to such a degree that the time-averaged heat transfer is positive.
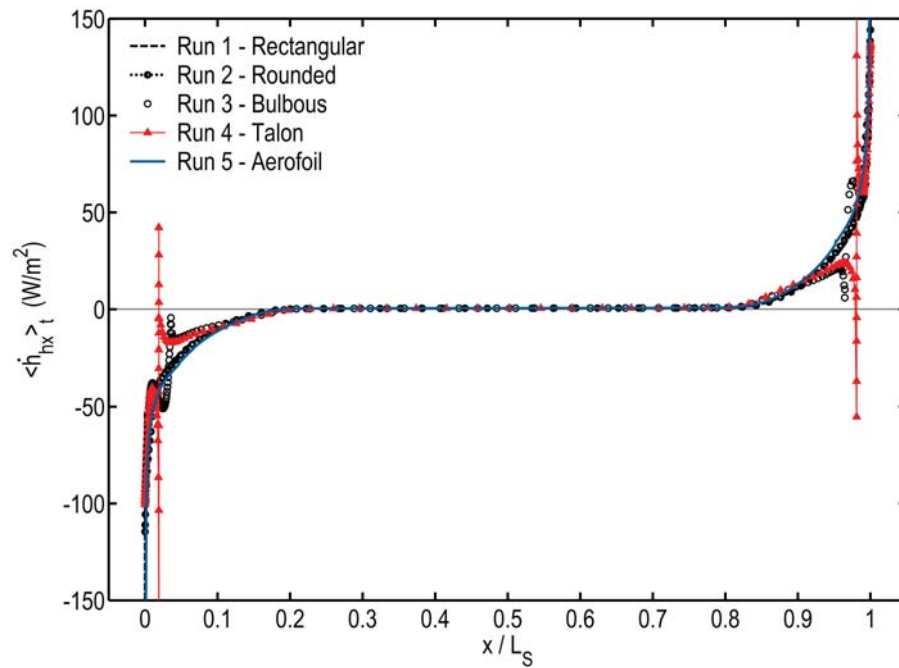
Figure 5.14: Distribution of time-averaged heat flux across the stack plate surface $\langle \dot{h} \rangle_t$ for normalised axial position x/L_S for a drive ratio of 1.7% (Runs 1 to 5).
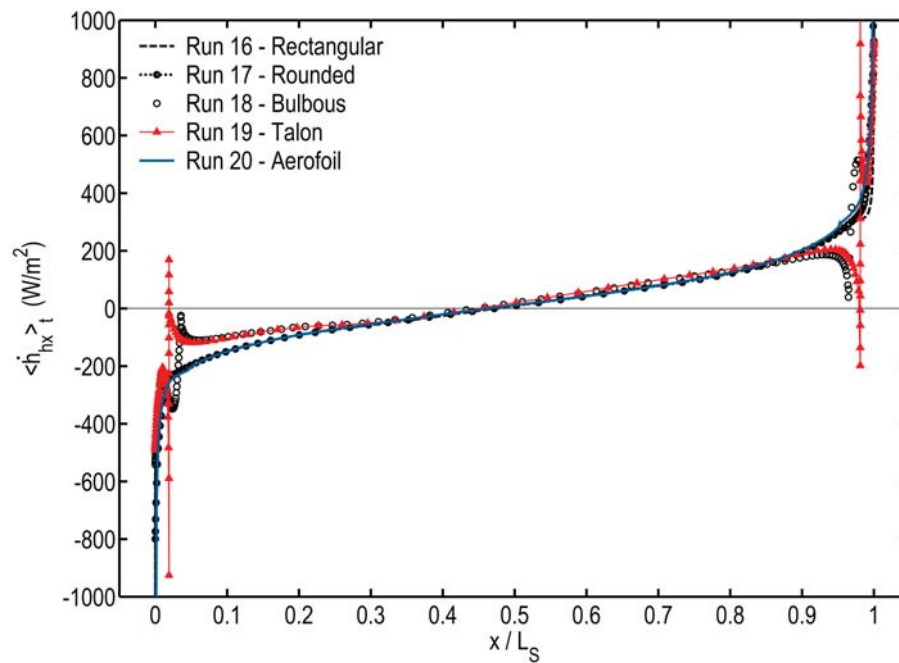

Figure 5.15: Distribution of time-averaged heat flux across the stack plate surface $\langle \dot{h} \rangle_t$ for normalised axial position x/L_S for a drive ratio of 6.8% (Runs 15 to 20).
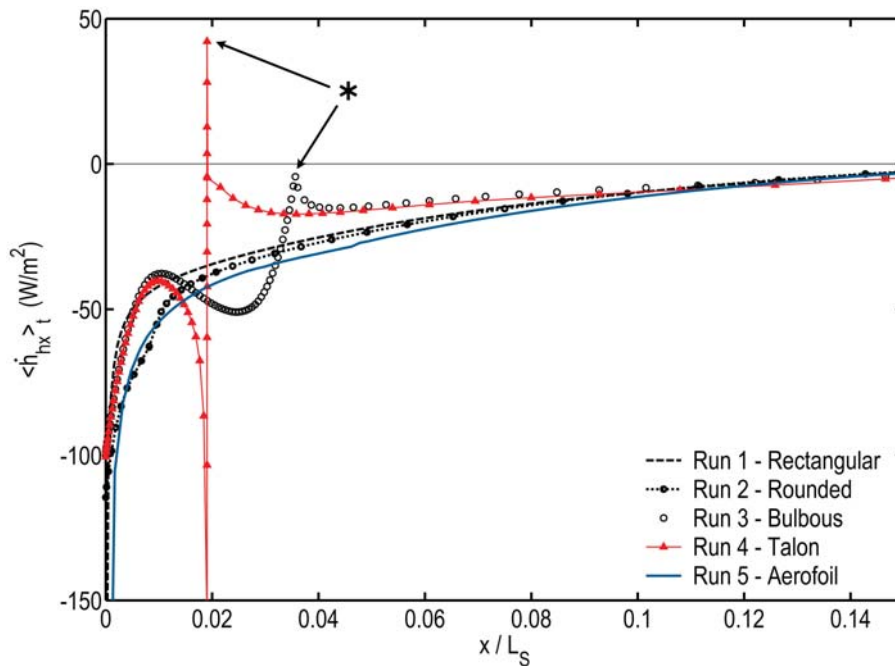
Figure 5.16: Distribution of time-averaged heat flux as per Figure 5.14 showing increased detail near the 'cold' end of the thermoacoustic couple. Runs 1 to 5 shown (DR of 1.7%). Distortions in $\langle \dot{h} \rangle_t$ due to sudden bends in the shapes of the Talon and Bulbous modelspaces are highlighted ($*$).
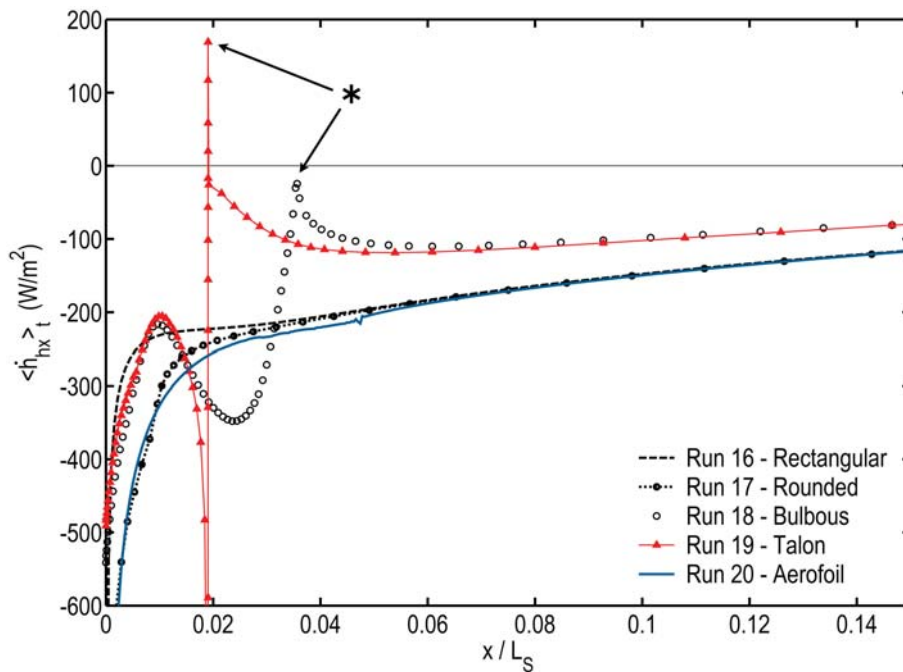

Figure 5.17: Distribution of time-averaged heat flux as per Figure 5.15 showing increased detail near the 'cold' end of the thermoacoustic couple. Runs 15 to 20 shown (DR of 6.8%). Distortions in $\langle \dot{h} \rangle_t$ due to sudden bends in the shapes of the Talon and Bulbous modelspaces are highlighted ($*$).
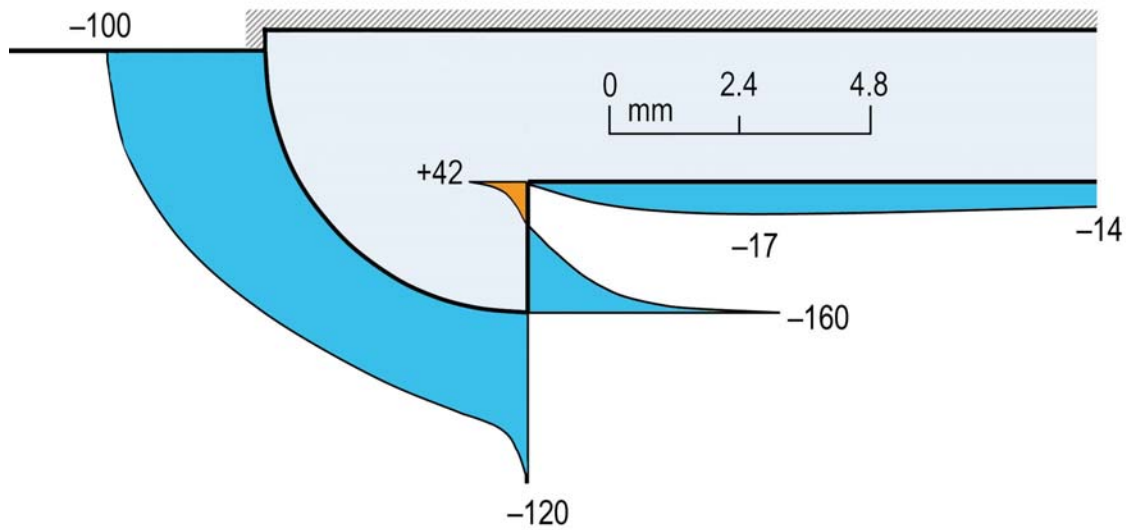
Figure 5.18: Sketch indicative of time-averaged heat flux $\langle \dot{h}_{hx} \rangle_t$ (W/m^2) across the cold end of Run 4 (Talon edge). Drive ratio is 1.7%.
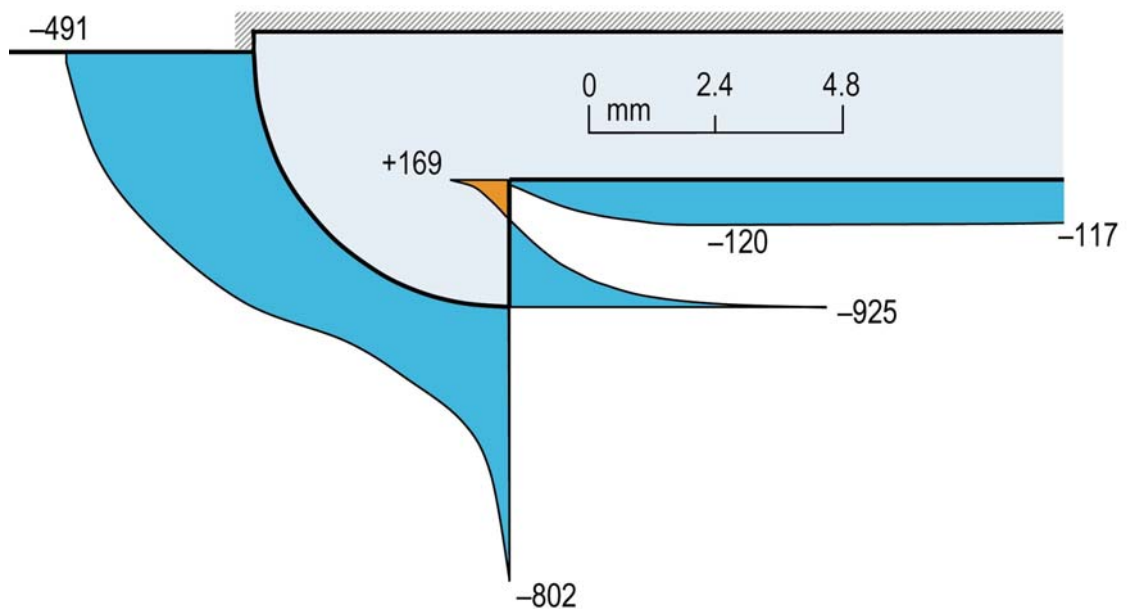

Figure 5.19: Sketch indicative of time-averaged heat flux $\langle \dot{h}_{hx} \rangle_t$ (W/m^2) across the cold end of Run 19 (Talon edge). Drive ratio is 6.8%.

The performance deficiency in the 'crevices' of the Talon and Bulbous edge shapes is thought to be due to the induced flow recirculation caused by the enlarged edge shape upstream. Singularities at the vertices of the Talon stack edge profiles shown in Figures 5.18 and 5.19 are provided for comparison only as the grid mesh profiles used in both Run 4 and 19 are identical.

When the prevailing flow of fluid is moving rightward, the flow conditions at the left end of the stack for the Talon edge profile are such that a local zone of recirculation forms inside the stack and behind the protrusion (Figures 5.8(a) and 5.8(b)), promoting increased contact with the stack plate but also reducing net flow towards the right end of the stack and introducing viscous heating. Heat stored in the protrusion from the phase immediately preceding may then be transferred to cooler gas deep inside the stack which is drawn leftward into the recirculation (Figure 5.8(c)). This mechanism is believed to exist for even the Rectangular edge shape, where flow over the leading edge creates a similar recirculatory recirculation zone, although its impact is less noticeable. This mechanism was not observed with the Rounded stack plate edge shape, suggesting that rounding off the edges of the stack plate will eliminate the described loss mechanism.

5.3.3 Cooling power

A comparison of the effective cooling power $\dot{Q}_{S,\text{cold}}$ of each stack plate edge shape is presented in Figure 5.20. This figure shows that only the Rounded edge profile consistently draws greater $\dot{Q}_{S,\text{cold}}$ compared to the Rectangular edge shape. Interestingly, all four alternatives considered outperformed the benchmark Rectangular edge shape profile at a drive ratio of 1.7%. However, the performance of the Talon and Bulbous variants underperformed at higher drive ratios when using $\dot{Q}_{S,\text{cold}}$ as a performance metric. It can also be seen in Figure 5.20 that the Talon and Bulbous

edge shapes require higher acoustic power inputs to achieve the same drive ratio because of the lower blockage ratio (higher acoustic impedance) presented by these stacks.
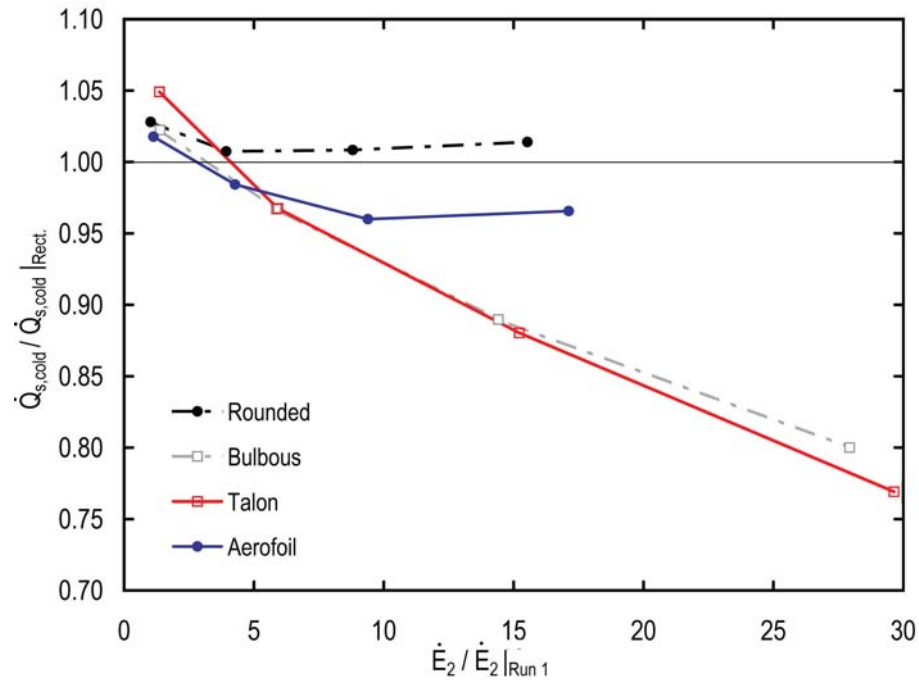

Figure 5.20: Effective cooling power $\dot{Q}_{S,\mathrm{cold}}$ (normalised using rectangular edge shape result) versus normalised $\dot{E}_2$.

Further to the result presented in Figure 5.20, the COP of each plate edge shape as defined in Equation (5.10) versus drive ratio is presented in Figure 5.21. It is quite clear from this figure that the Talon and Bulbous edge shapes are undesirable from an efficiency viewpoint when compared to the Rectangular and Rounded edge shape. The Rounded edge shapes is shown to provide the highest COP of the edge shape variants considered. Although achieving a higher $\dot{Q}_{S,\mathrm{cold}}$ for a drive ratio of 1.7%, the Aerofoil edge shape did not achieve a COP as high as the Rounded or Rectangular edge shapes, due to the increased acoustic power input required, and a relatively lower $\dot{Q}_{S,\mathrm{cold}}$. Above a drive ratio of 1.7%, the relative acoustic power input for the Aerofoil edge shape profile reduces significantly compared to the Rectangular edge shape profile. However, this is negated by continued deficiency in
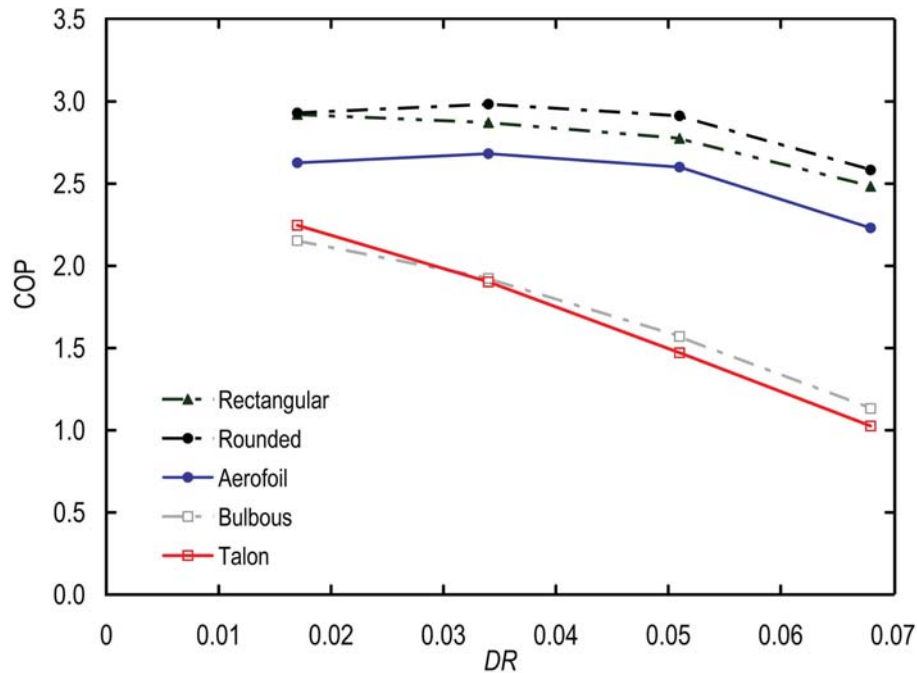
Figure 5.21: Coefficient of performance COP versus drive ratio for all edge shape profiles considered in this study.

$\dot{Q}_{S,\text{cold}}$, and the COP of the Aerofoil edge shape profile is always lower than that obtained using the Rectangular stack edge profile (Figure 5.21) for the drive ratios modelled.

5.3.4 Temperature distributions

Figure 5.22 presents the gas temperature difference across the thermoacoustic couple, normalised by the gas temperature difference achieved using a rectangular plate, versus drive ratio. This figure shows that for each drive ratio considered, the Aerofoil edge shape is able to generate a higher gas temperature difference between the left and right ends of the plate, $\Delta T_{k,hx}$, than the Rectangular edge shape, despite a lower COP, as shown in Figure 5.21. Shifting from a rectangular shaped stack plate to a rounded edge plate is expected to result in a $\Delta T_{k,hx}$ reduction of up to 8%, and if using Talon or Bulbous edge shapes, up to 35%.
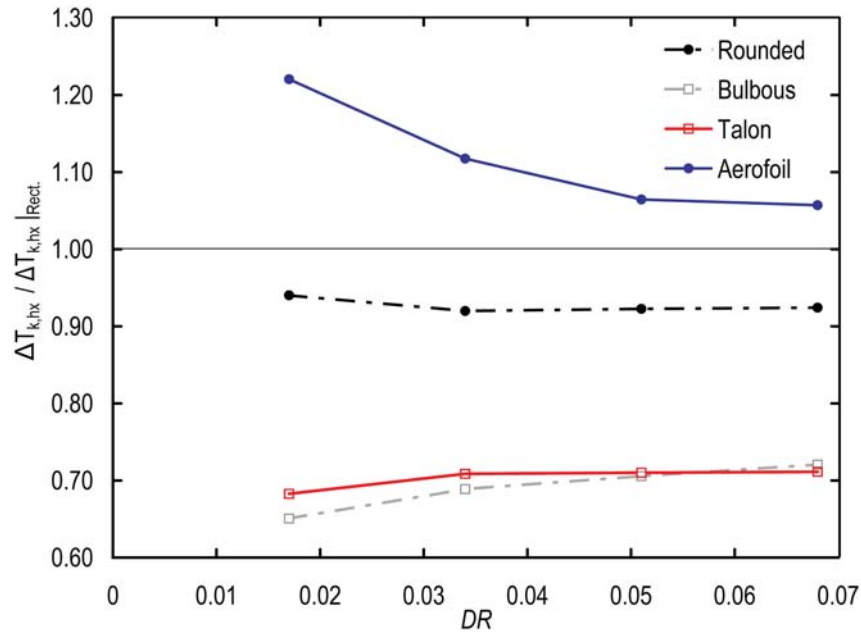
Figure 5.22: Normalised $\Delta T_{k,hx}$ versus drive ratio for various edge shape conditions.

This result was explored further, on the basis that whilst $\Delta T_{k,hx}$ is a useful measure of performance, it may not include actual temperature extremes if the axial positions at which the minimum and maximum temperatures develop do not correspond with the left and right stack plate edges. It is reasonable to assume that design of thermoacoustic devices involving heat exchangers and a stack will locate the heat exchangers directly up against each end of the stack, and that automatic fine 'tuning' of the axial position of the heat exchangers is unlikely beyond the design phase.

Using a Rectangular edge shape with increasing drive ratio, the time-averaged gas temperature $\langle T_k \rangle_t$ on the mid-plate line ($y{=}0$) is presented in Figure 5.23 for increasing drive ratios. The $\Delta T_{k,hx}$ result is calculated using values obtained on x/L_S equal to 0 and 1, and is considered to be an accurate measure of the gas temperature extremes if the minima and maxima of T_k are obtained on these values of x/L_S. This is observed at most of the drive ratios simulated, but at a drive ratio of 1.7%, the minimum and maximum values of $\langle T_k \rangle_t$ lie at x/L_S equal to
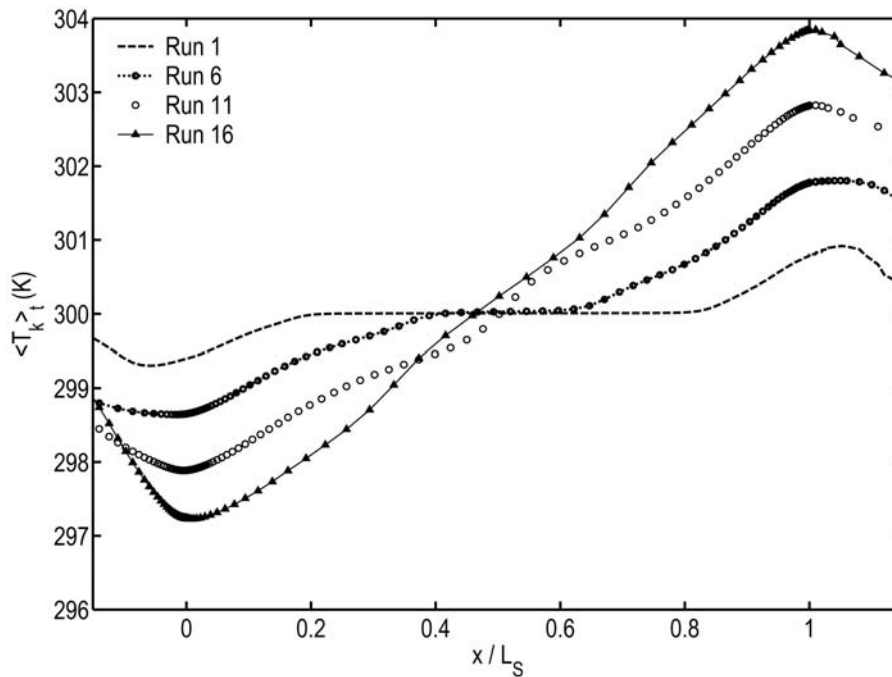
Figure 5.23: Time-averaged gas temperature T_k for the Rectangular edge shape model versus axial position normalised by stack length for drive ratios 1.7% (Run 1) to 6.8% (Run 16). The stack plate edges are marked with vertical lines at x/L_S equal to 0 and 1.

approximately -0.05 and 1.05 respectively, suggesting that $\Delta T_{k,hx}$ understates the performance of the thermoacoustic couple at this drive ratio. Note that as the drive ratio is increased for the Rectangular edge shape, the temperature distribution on $y=0$ approaches a straight line within the stack (Run 16 shown in Figure 5.23).

Figure 5.24 shows the distribution of $\langle T_k \rangle_t$ for various edge shapes for a drive ratio of 1.7%. The Talon and Bulbous edge shapes that were identifed previously as underperforming, are shown here to again be less effective in establishing a temperature differential between each end of the stack, with a plateau-like shape to the $\langle T_k \rangle_t$ distribution at each end. With the Rectangular and Rounded edge shapes achieving near identical distributions of $\langle T_k \rangle_t$, the Aerofoil edge shape clearly stands out. In Figure 5.25, which shows the same comparison except at a higher drive ratio of 5.1%, the trend is continued if one considers the 'cold' end of the device only.
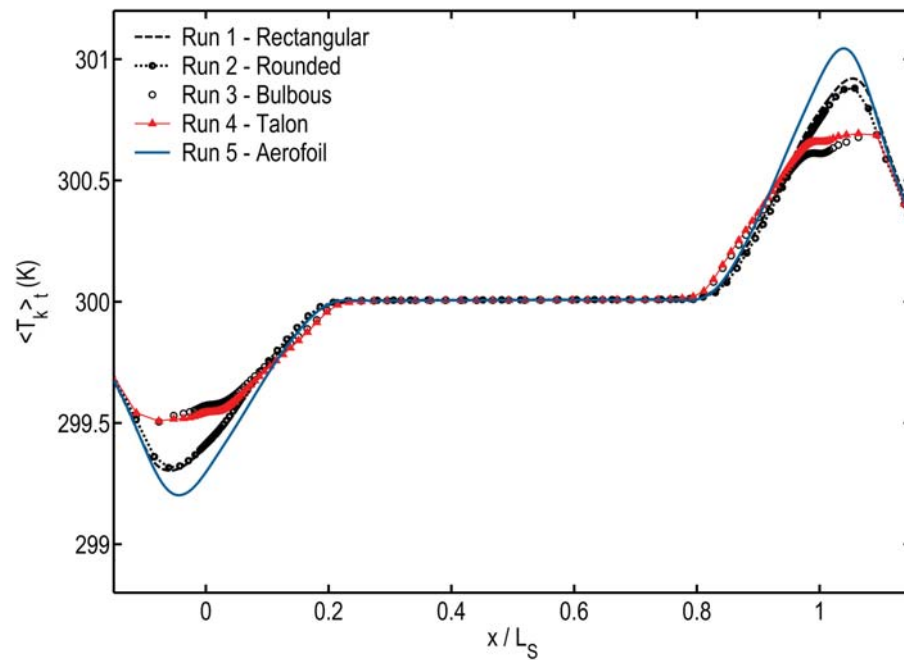
Figure 5.24: Time-averaged gas temperature $\langle T_k \rangle_t$ versus axial position normalised by stack length for selected edge shape conditions. Runs 1 to 5 are presented for which the drive ratio is common and equal to 1.7%.
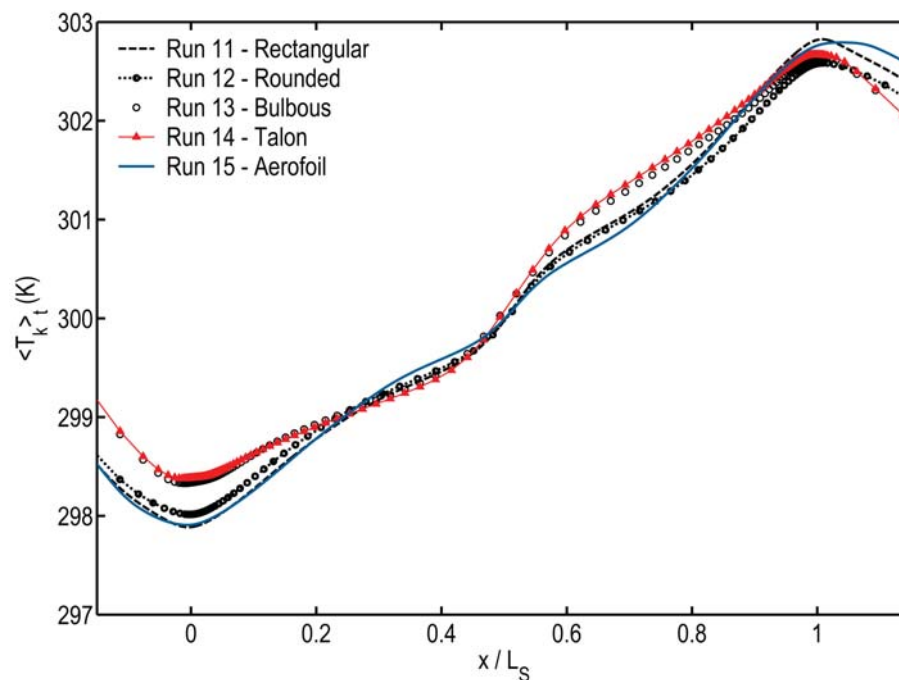

Figure 5.25: Time-averaged gas temperature $\langle T_k \rangle_t$ versus axial position normalised by stack length for selected edge shape conditions. Runs 11 to 15 are presented for which the drive ratio is common and equal to 5.1%.

The same cannot be said for the right or 'hot' end of the stack at this drive ratio. At a drive ratio of 5.1%, there are differences in the distribution of the time-averaged gas temperature at the right (hot) end of the stack for the five edge shapes modelled. It is difficult to conclude that one edge shape is more effective at this end than the others, but it may be stated that the maximum value of $\langle T_k \rangle_t$ is achieved by each edge shape at $x/L_S \approx 1$.

There is also a noticeable difference in performance between each end of the stack region, with the total rate of heat transfer at the 'hot' end being higher than at the 'cold' end. This result is attributed to viscous heating of the gas throughout the stack region.

5.4 Discussion and conclusions

The comparative performance of five thermoacoustic stack plate edge shapes has been estimated using numerical analysis. This study has endeavoured to address the third 'gap' identified in Section 2.4, namely the lack of knowledge with regards to the effectiveness and efficiency of thermoacoustic stack plates with non-rectangular edge shapes.

The results of the analysis indicate that the thermoacoustic couple edge profile has a significant impact on the overall performance. The influence of stack edge shape upon the flow impedance of the stack is an important consideration when comparing alternative stack edge shapes. The 'sleeker' aerofoil and rounded edge shapes with lower flow resistance are preferable designs, since both the acoustic impedance on the inlet boundary and the effective cooling rate $\dot{Q}_{S,\mathrm{cold}}$ were more desirable than other edge shapes considered.

Although the Talon and Bulbous edge shapes are expected to generate a higher

rate of heat transfer across the stack face for similar acoustic power inputs at low drive ratios, the same cannot be said for these edge shapes at higher drive ratios. The Talon and Bulbous profiles also do not achieve as high temperature difference, cooling power or efficiency values as the alternative profiles when using the defined parameters $\Delta T_{k,hx}$, $\dot{Q}_{S,\mathrm{cold}}$ and COP.

It remains to be seen if stacks with combinations of stack edges (e.g. one edge 'Rounded', the other 'Aerofoil' or 'Rectangular') would have improved performance.

On the basis of the results from this study, rounding the edges of a rectangular stack section is expected to yield improvements in the effective cooling rate and COP. Shifting to an aerofoil-like stack section is less preferred because of the minimisation of heat transfer surface area at each edge, and perhaps the increased complexity in manufacture. Of the edge shape profiles considered in this study, the Rounded edge shape profile strikes the most effective balance of heat exchange area and edge taper. These properties have demonstrated a minimisation of acoustic streaming on the inside face of the stack, and increased $\dot{Q}_{S,\mathrm{cold}}$ by greater retention of stack thickness at the plate extremities to yield a greater overall COP. On this basis, the Rounded edge shape profile is recommended for thermoacoustic stack plates in practical devices.

The next chapter will investigate the phenomenon of acoustic streaming in thermoacoustic stacks and compare experimental data with numerical predictions of thermoacoustic couples.